J Mater Sci (2023) 58:2676–2688

Electronic materials

Construction of g-C_3N_4 nanoparticles modified TiO_2 nanotube arrays with Z-scheme heterojunction for enhanced photoelectrochemical properties

Fengling Zhang[1,2], Jianxing Liu[1,2], Hongrui Yue[1,2], Gongjin Cheng[1,2], and Xiangxin Xue[1,2,*]

[1] School of Metallurgy, Northeastern University, Shenyang 110819, China
[2] Liaoning Key Laboratory of Recycling Science for Metallurgical Resources, Shenyang 110819, China

Received: 26 March 2022
Accepted: 21 June 2022
Published online: 30 January 2023

ABSTRACT

Constructing heterojunction structures is an effective way to produce highly efficient photocatalysts with favorable charge transfer paths. In this study, TiO_2 nanotube arrays were synthesized using an electrochemical anodization method, and g-C_3N_4 nanoparticles were grown in situ on TiO_2 nanotubes using three thermal polymerization strategies. Compared with pure TiO_2, the g-C_3N_4/TiO_2 heterojunctions exhibited different degrees of enhancement in photoelectrochemical performance under stimulated solar light. The TNT-L heterojunction fabricated by urea solution exhibited excellent photoelectrochemical (PEC) activity and followed a Z-scheme mechanism, which is beneficial for carrier separation and maintaining the original redox capacity of each component. The crystallinity, morphology, chemical composition, and optical properties of the photocatalysts were also analyzed using a series of characterization techniques.

Introduction

Semiconductor photocatalytic technology for solar energy conversion and contamination control has received widespread attention in recent years due to its prospects in promoting environmental restoration and alleviating the energy crisis [1, 2]. Since the photoelectrochemical splitting of water by TiO_2 electrodes was first reported in 1972, the semiconductor TiO_2 has received intensive research as a promising photoactive material in the fields of contaminant degradation, hydrogen generation, and solar cells due to its strong redox ability and high photocatalytic activity under ultraviolet irradiation [3, 4]. In particular, TiO_2 with one-dimensional nanostructures (nanotubes, nanorods, nanowires, etc.) has drawn considerable interest owing to the faster axial charge transport path, high aspect ratio for light harvesting, and large surface area for

Handling Editor: Kyle Brinkman.

Address correspondence to E-mail: xuexx@mail.neu.edu.cn
E-mail Address: 153620969@qq.com

https://doi.org/10.1007/s10853-022-07730-7

accessible active sites [5]. However, TiO_2 suffers from inherent drawbacks, such as a wide bandgap and relatively high recombination rate of photogenerated electrons and holes [6, 7]. Therefore, many efforts are dedicated to improve the electric structure of TiO_2 to increase the optical response and charge separation efficiency. One of the most effective approaches is coupling with staggered band structure configuration semiconductors to form heterojunctions [8–11].

As a visible-light-driven π-conjugative polymer semiconductor, graphitic carbon nitride (g-C_3N_4) possesses an appropriate band structure and good physicochemical stability, making it an attractive candidate for reductive reactions (H_2 evolution and CO_2 reduction) and oxidative degradation [12–14]. However, the photocatalytic activity of g-C_3N_4 is unsatisfactory owing to its low quantum efficiency [15]. Due to the well-matched energy band structure between TiO_2 and g-C_3N_4, many studies have constructed organic–inorganic g-C_3N_4/TiO_2 heterojunctions to restrain the respective drawbacks of each component and realize synergistic effects in promoting charge generation and separation [16–18]. The interface properties between semiconductors are critical for the charge carrier transfer [19]. Among various synthesis methods, the in situ growth strategy favors the formation of strong interactions and intimate contact interfaces between components to reduce charge transfer impedance.

In this study, photocatalysts composed of g-C_3N_4 nanoparticles and highly ordered TiO_2 nanotube arrays were fabricated through three thermal polymerization strategies. Herein, g-C_3N_4 was grown on the surface of TiO_2 nanotubes to form a tight two-phase contact layer, which facilitated the spatial separation of photogenerated carriers. The synergistic effect formed between g-C_3N_4 nanoparticles and TiO_2 nanotubes was investigated by various characterization techniques and photoelectrochemical measurements, and the mechanism of charge separation and transfer was proposed. The construction of g-C_3N_4/TiO_2 heterojunctions may provide promising prospects for water-splitting photoelectrodes.

Experimental method

Preparation of TiO_2 and g-C_3N_4/TiO_2 samples

Synthesis of TiO_2 nanotube array membranes: Commercial pure titanium sheets (Φ 30*2 mm) were polished first, and then ultrasonically cleaned with deionized water and ethanol. The TiO_2 nanotube array membrane was prepared by a two-step electrochemical anodic oxidation method with a direct current power supply. First, the titanium sheet was oxidized at 60 V for 2 h in an electrolyte solution containing ethylene glycol and 0.5 wt% ammonium fluoride. Then, the cleaned specimen was oxidized in ethylene glycol solution containing 0.5 wt% ammonium fluoride and 0.6 vol% hydrofluoric acid at 60 V for 4 h. Finally, the amorphous precursor was calcinated at 450 °C in the air for 1 h to crystallize.

Synthesis of g-C_3N_4 functionalized TiO_2 nanotubes: Three strategies were used to fabricate g-C_3N_4/TiO_2 nanocomposites. Method I: As a novel synthesis approach, g-C_3N_4 was grown on TiO_2 nanotubes by gasification conversion of urea solution. A schematic diagram of the synthesis procedure is shown in Fig. 1. The anodized TiO_2 nanotube array membrane was placed on the top of a crucible containing the liquid phase precursor (2 g urea, 2 ml H_2O), and then, the crucible was calcinated at the temperature of 500 °C for 1 h in a tubular furnace under an air

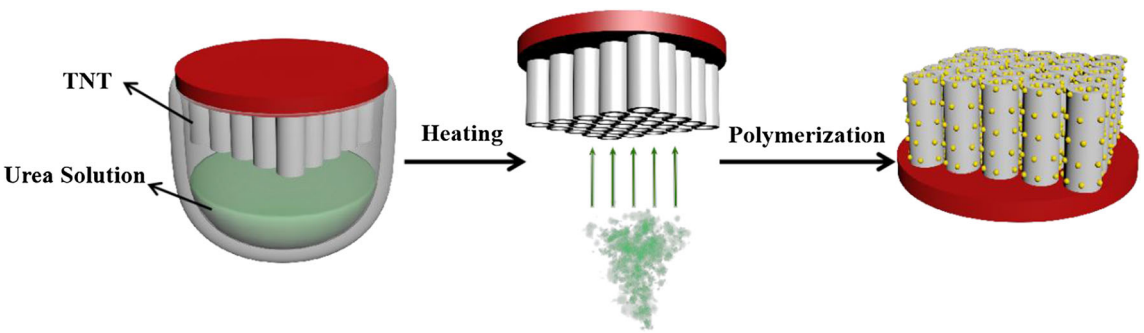

Figure 1 Schematic diagram for the fabrication of the TNT-L sample.

atmosphere at a heating rate of 4 °C min^{-1}. The final product was denoted as TNT-L. Method II: The g-C_3N_4 was deposited onto TiO_2 nanotubes through the solid urea sublimation and conversion. Two grams of urea was placed in a crucible covered with TiO_2 nanotube arrays, and the calcination process was the same as that described above for TNT-L. Concurrently, a certain amount of g-C_3N_4 powder was also obtained in the bottom of the crucible after calcination. This nanocomposite was denoted as TNT-S. Method III: The deposition of g-C_3N_4 into TiO_2 nanotube arrays was performed using the vacuum impregnation method. The prepared TiO_2 nanotube coating was immersed in urea aqueous solution with a concentration of 1 g mL^{-1} for 24 h under vacuum conditions. Then, the TiO_2 nanotube arrays were directly calcinated with the same procedure above, and the resultant sample was denoted as TNT-I.

Characterization

Phase composition and crystallinity were analyzed by an X-ray powder diffractometer (Philips X'Pert PRO, Netherlands) using Cu-Kα radiation over a 2θ range of 10–80°. The surface chemical compositions of the samples were detected by an X-ray photoelectron spectrometer (Thermo Fisher ESCALAB 250Xi, USA) with a monochromatized Al-Kα excitation source (hv = 1486.8 eV), and all the binding energy values were calibrated based on C 1 s at 284.8 eV as a reference. Morphology features and microstructures were investigated by a scanning electron microscope (S4800, Japan) equipped with an energy dispersive X-ray spectroscope to examine the elemental composition. Ultraviolet–visible diffuse reflectance spectra were measured against a $BaSO_4$ reference in the region of 270–800 nm using a UV–Vis absorption spectrophotometer (UV2550, Japan). ESR measurements were performed at ambient temperature using an EMXmicro A300 spectrometer. Photoluminescence (PL) spectra were collected on a fluorescence spectrophotometer (Edinburgh FLS1000, U.K.) at room temperature.

PEC Measurements

Photoelectrochemical (PEC) performance was measured with a CHI650 electrochemical workstation (Chenhua Co. Ltd, Shanghai) in a three-electrode system. The as-fabricated samples were directly used as working electrodes with an active area of 1 cm^2. Platinum sheets and saturated Ag/AgCl electrodes were employed as the counter and reference electrodes, respectively. All the measurements were performed in a 1 M KOH electrolyte solution. A 500 W xenon lamp was acted as the simulated solar light source to provide full-spectrum illumination with a 100 mW cm^{-2} light intensity. The potential values versus Ag/AgCl electrode were converted to reversible hydrogen electrode potential (RHE) by the Nernst equation. Linear sweep voltammetry curves were recorded at a scanning rate of 10 mV s^{-1}. The transient photocurrent responses of the samples were recorded at intervals of chopping light irradiation under a fixed bias voltage of 0 V versus Ag/AgCl electrode. Electrochemical impedance spectra (EIS) were measured with an amplitude of 5 mV, and a frequency range of 10^{-2}–10^5 Hz under open-circuit voltage conditions.

Results and discussions

Characterization analysis

Figure 2 shows the X-ray diffraction (XRD) patterns of the as-synthesized samples. For pure g-C_3N_4, the primary characteristic diffraction peak located at 27.4° corresponded to the (002) plane with an interlayer stacking structure and indicated good

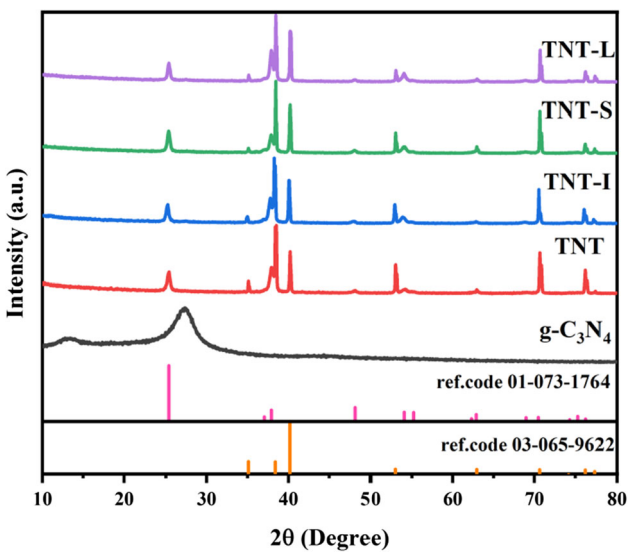

Figure 2 XRD patterns of g-C_3N_4, TNT, TNT-I, TNT-S, and TNT-L samples.

crystallinity. The weak peak at a low angle diffraction of 13.3° was attributed to the (100) plane with an in-plane structure of tri-s-triazine units [20, 21]. Comparing TiO_2 and nanocomposites, there were no obvious phase structure differences in the XRD patterns. The diffraction reflections located at 25.33°, 37.84°, 48.07°, 53.95°, 55.11°, and 62.75° were indexed to the crystal planes (101), (004), (200), (105), (211), and (204) of anatase TiO_2 (JCPDS card 01–084-1286) [22]. Except for anatase TiO_2, the other diffraction peaks originated from the Ti substrate (JCPDS card 01–089-4893) with strong intensity. The characteristic diffraction peak of g-C_3N_4 in the composites was not obvious due to the relatively lower crystallization and percentage content.

The surface morphology and structure of TiO_2 nanotubes, g-C_3N_4, and g-C_3N_4/TiO_2 composites were characterized by scanning electron microscopy and transmission electron microscopy. As shown in Fig. 3a, the top view image of the TiO_2 photoelectrode consisted of a distinct microscopic-ordered tubular structure. The pure g-C_3N_4 sample exhibited an irregular flake morphology in submicron size (Fig. 3b).The TNT-I and TNT-S samples (Fig. 3c and d) show that g-C_3N_4 nanoparticles occurred on the upper surface of TiO_2 nanotubes, and some blocked the nanotube orifices after thermal polymerization. Figure 3e, f shows the SEM images of TNT-L at different magnifications. The g-C_3N_4 nanoparticles were uniformly and tightly anchored on the TiO_2 nanotube surfaces. The TiO_2 nanotubes not only acted as platforms, but also effectively suppressed the agglomeration and size growth of g-C_3N_4 nanoparticles. The pore size of the nanotubes was statistically calculated using Image J software, and each aperture was represented by an equivalent diameter. Results are shown in Fig. S1. The equivalent diameter distribution showed that the TNT-L sample has pore sizes ranging from 70 to 160 nm, while 100 ~ 130 nm were the majority. To identify the spatial distribution of g-C_3N_4 on the TiO_2 nanotubes, the corresponding energy-dispersive spectroscopy (EDS) mappings of the TNT-L sample are shown in Fig. S2 and Fig. S3. It can be seen from Fig. S2 that Ti, O, C, and N elements were homogeneously distributed on the top of the nanotubes. The side-view images of TNT-L (Fig. S3) showed that the g-C_3N_4 nanoparticles were uniformly anchored on the walls of nanotubes, which further confirmed that g-C_3N_4 nanoparticles were loaded on the entire TiO_2 nanotubes to form a heterojunction structure.

The morphological and structural characteristics of the samples were analyzed by transmission electron microscopy, and the TEM and HRTEM results are shown in Fig. 4. Figure 4a shows that the TiO_2 nanotubes were dense and uniformly arranged, and the g-C_3N_4 nanoparticles formed by thermal polymerization were deposited onto the walls of TiO_2 nanotubes (Fig. 4b), which was consistent with the SEM images. The selected electron diffraction pattern (SADE) of a typical area is shown in Fig. 4c. The diffraction rings matched the (101), (107), (101), (107), (217), (228), (424), and (0012) interplanar spacings of anatase TiO_2. The HRTEM image of TNT-L is shown in Fig. 4d, and the corresponding Fourier transform (FFT) of the region A is shown in Fig. 4e. Each crystal plane was determined after calibrating the FFT results, and the marked interplanar spacing was measured to be approximately 0.1736 nm, which was in good agreement with the interplanar spacing corresponding to the anatase TiO_2 (105) plane.

The surface chemical compositions of TiO_2 and the composites were studied by X-ray photoelectron spectroscopy (XPS), as shown in Fig. 5. Figure 5a shows the high-resolution Ti 2p spectra, with binding energies of 458.5 and 464.3 eV that were attributed to Ti $2p_{3/2}$ and Ti $2p_{1/2}$ of Ti^{4+} in anatase TiO_2. Compared with bare phase TiO_2, the characteristic peaks of Ti 2p in TNT-I, TNT-S, TNT-L shifted to lower binding energy regions, which indicated that the electron cloud density of Ti was changed because of the interfacial interaction between TiO_2 and g-C_3N_4 [23, 24]. From the O 1 s spectra (Fig. 5b), the primary peak at 529.7 eV in the TNT sample could be attributed to the oxygen lattice in TiO_2, and the binding energy in the composites exhibited a negative shift, as in the case of the Ti 2p spectrum. The marginal peak located at 531.2 eV corresponded to -OH functional groups at the surface [25, 26]. The C 1 s spectra (Fig. 5c) of the samples showed three peaks, the peak centered at 284.8 eV arising from C–C coordination or adventitious carbon, while the peaks at 286.3 and 288.3 eV were identified as sp2 hybridized carbon in N-containing carbon aromatic ring [22, 25]. Also, the N 1 s spectra (Fig. 5d) could be deconvoluted into two Gaussian peaks, indicating two types of N bonding. The dominating peak at 397.9 eV was related to pyridinic nitrogen (C-N = C) in triazine rings, and the peak at 399.7 eV was derived from pyrrolic

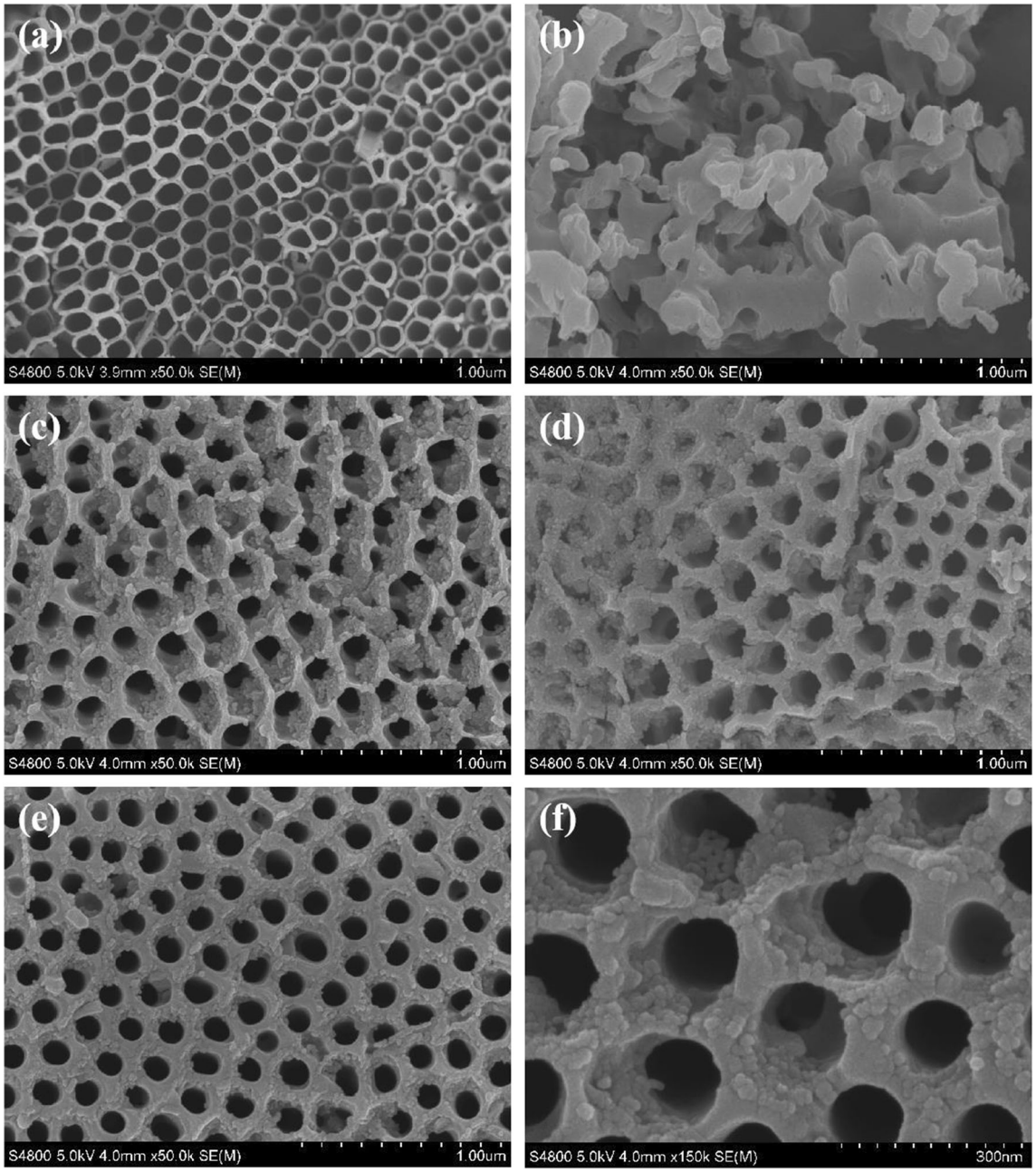

Figure 3 SEM images of TNT (**a**), g-C_3N_4(**b**), TNT-I (**c**), TNT-S (**d**), and TNT-L (**e**, **f**) at different magnifications.

nitrogen (N-$(C)_3$) [27]. Comprehensive analysis of XPS results demonstrated the existence of heterojunction structures in the composites, and the intimate interfacial interaction between TiO_2 nanotubes and g-C_3N_4 nanoparticles may improve the photocatalytic activity.

PEC performance

A series of PEC measurements were performed to study the optoelectronic properties of the as-prepared TiO_2 and g-C_3N_4/TiO_2 photoelectrodes. The carrier characteristics at the interface of the semiconductor and electrolyte were assessed by linear sweep voltammetry. Figure 6a shows the variation in current densities versus applied potential (I–V) in the dark and under illumination conditions. The dark

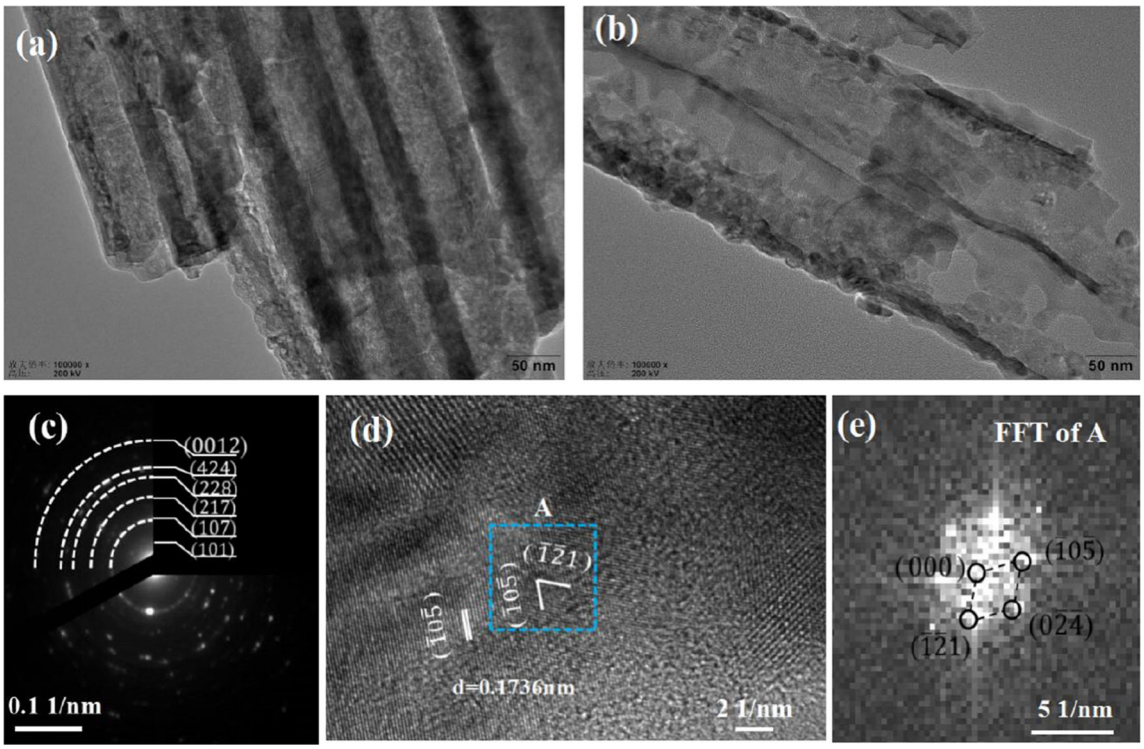

Figure 4 TEM images of TNT (**a**), TNT-L (**b**), and HRTEM and SAED patterns of TNT-L sample (**c–e**).

current densities for all the samples were negligible, while a pronounced photoresponse was observed upon illumination, implying effective light-harvesting and charge separation. The incidence of light led to the generation of electron and hole pairs in the semiconductor. The photoexcited e^- moved from the conduction band to external circuit through the electrode, while the holes would ionize water molecules to produce H^+ ions. Hydrogen ions were transported to the counter electrode through the electrolyte and recombined with electrons from the external circuit to generate hydrogen; the carrier migration was proportional to the amount of hydrogen produced by water splitting [23, 28]. Therefore, the photocurrent information was used to evaluate the effectiveness of semiconductor photocatalysts for water splitting. It was obvious from I–V curves that the photocurrent densities showed a general order of TNT-L > TNT-S > TNT-I > TNT. The corresponding photoconversion efficiency (η) of each photoelectrode was calculated by the following equation:

$$\eta(\%) = I\left(E^0_{rev} - V_{app}\right)/J_{light} \quad (1)$$

where E^0_{rev} is the standard reversible potential (1.23 V vs. RHE), I is the photocurrent density (mA cm^{-2}), V_{app} is the applied bias potential versus RHE, and J_{light} is the incident light intensity (mW cm^{-2}). Plots of the photoconversion efficiency versus applied bias potentials are presented in Fig. 6b. The optimal photoconversion efficiency of TNT achieved 0.36% at -0.66 V vs. Ag/AgCl. With the introduction of g-C_3N_4 into TiO_2 nanotubes, the photoconversion efficiency of TNT-I and TNT-S increased to 0.52% and 0.59%, respectively. In particular, TNT-L generated the highest photoconversion efficiency of 0.66% among all the samples, which was approximately 1.83 times higher than that of pure TiO_2 nanotubes. Thus, coupling g-C_3N_4 is an effective strategy to improve the photocurrent density and photoconversion efficiencies of TiO_2.

To evaluate the transient photoresponse of the as-prepared electrodes, amperometric photocurrent density versus time (I–t) measurements were performed at 0 V vs. Ag/AgCl under on/off light illumination. Figure 7a shows that the photocurrents of all four electrodes underwent a marked increase in irradiation, and then, the current density immediately decreased in the dark, indicating the fast separation rate of photoelectrons and holes [29]. The stable photocurrents of TNT, TNT-I, TNT-S, and TNT-L under illumination after ten cycles were 0.47, 0.72, 0.78, and 0.87 mA cm^{-2}, respectively. To verify

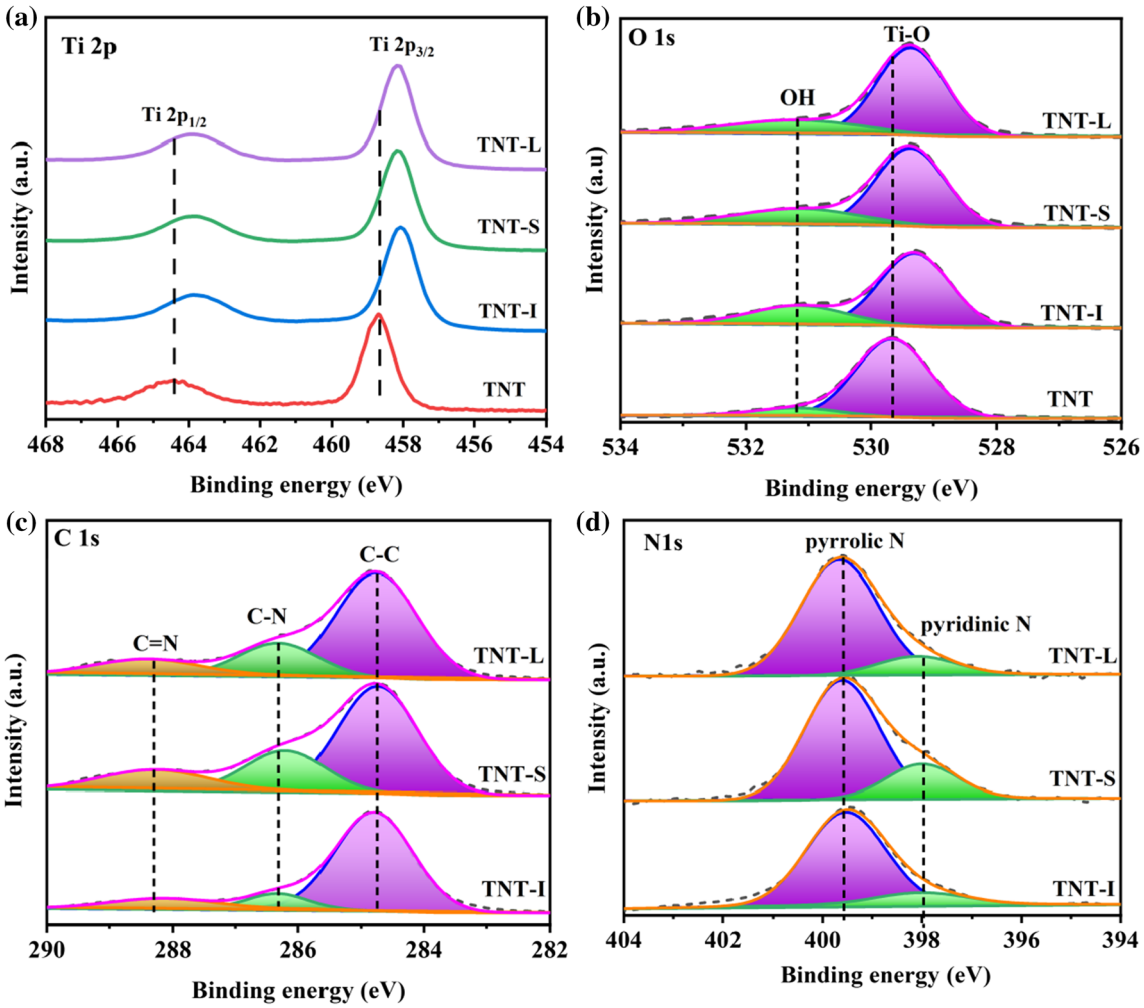

Figure 5 XPS survey spectra of samples: Ti 2p (**a**), O 1 s (**b**), C 1 s (**c**), and N 1 s (**d**).

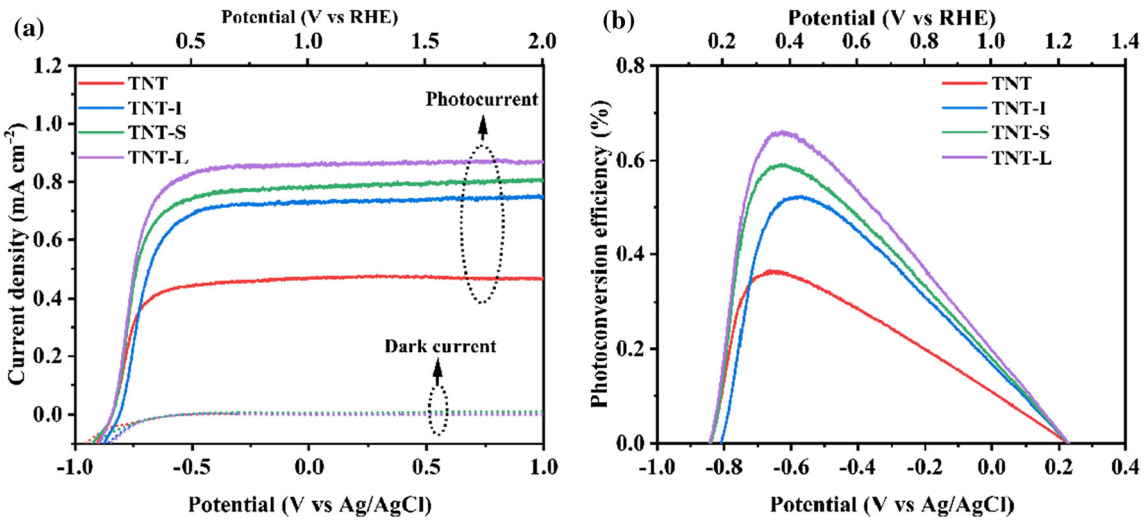

Figure 6 Linear sweep voltammetry curves under dark and illumination (**a**); Photoconversion efficiency under different applied potential (**b**).

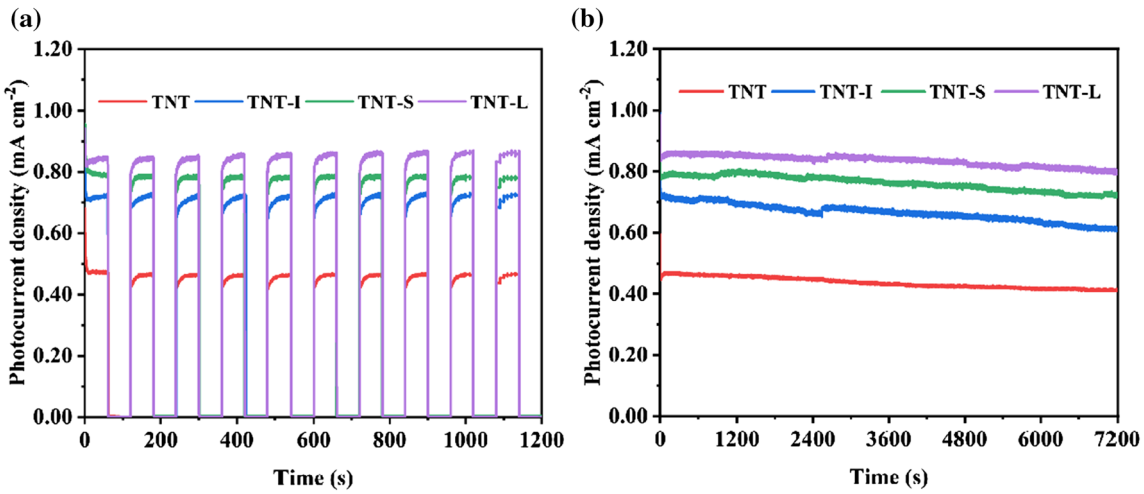

Figure 7 Transient photocurrent responses with 60 s cycles (**a**); Photocurrent density under constant illumination (**b**).

the stability of the electrodes, the corresponding *I–t* curves were measured at 0 V vs. Ag/AgCl for a constant time over 7200 s. As shown in Fig. 7b, the photocurrent density of all four samples showed a slight attenuation after the test, which confirmed that the prepared electrodes possessed good stability.

The charge transfer behavior at the electrode and electrolyte interface was investigated using electrochemical impedance spectroscopy. EIS measurements were performed under light irradiation at the open-circuit potential, and the results and simulated equivalent circuit model are shown in Fig. 8. The Nyquist plots for all electrodes consist of semicircles at high frequencies and oblique lines in the low-frequency region. The semicircle is correlated to the charge transfer resistance (*R*ct) at the electrode/electrolyte interface, while the oblique line reflects the Warburg diffusion process (*Z*w) [30, 31]. Furthermore, the intersection of the semicircle with the real axis at high frequency was attributed to the internal resistance (*R*s) [32]. The Nyquist plots were fitted by Z-view software, and the impedance parameters are listed in Table S1. Among the four electrodes, nanocomposites electrodes exhibited a lower R_{ct} value than that of pure TiO_2, while TNT-L possessed the lowest interface resistance. Smaller R_{ct} values indicate a higher charge transport capability, which can markedly enhance PEC activity [33].

PEC mechanism of g-C_3N_4/TiO_2

Photoelectrochemical performance is closely related to the photoexcited property and charge separation

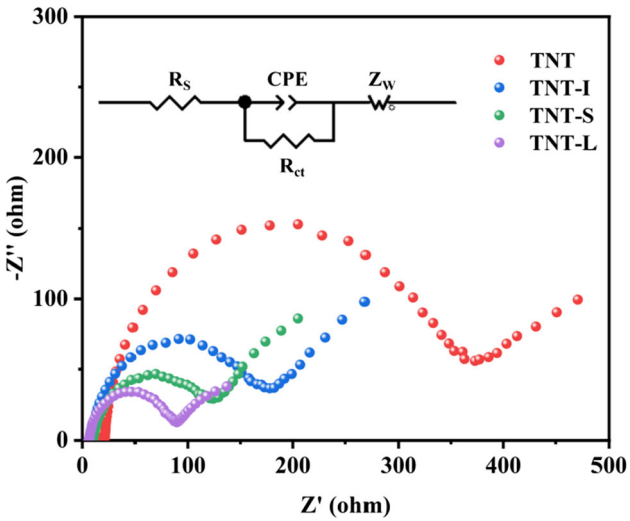

Figure 8 Nyquist plots of TNT, TNT-I, TNT-S, and TNT-L electrodes, and the equivalent circuit model inset.

ability of photocatalysts; thus, UV–vis diffuse reflectance and photoluminescence (PL) experiments were performed to understand the optical absorption behavior and carrier separation efficiency. The DRS spectra are shown in Fig. 9, and the corresponding band edges are given in the figure's insets. The TNT sample exhibited a spectral response in the UV region below 380 nm, while pure g-C_3N_4 can absorb light from the UV to visible range with a band edge absorption of ~ 470 nm. After combining TiO_2 with g-C_3N_4 in three thermal polymerization pathways, the light absorption edge of all composites showed a slight partial redshift in comparison with that of TNT. Additionally, the bandgap energies of TNT, TNT-I, TNT-S, TNT-L, and g-C_3N_4 estimated

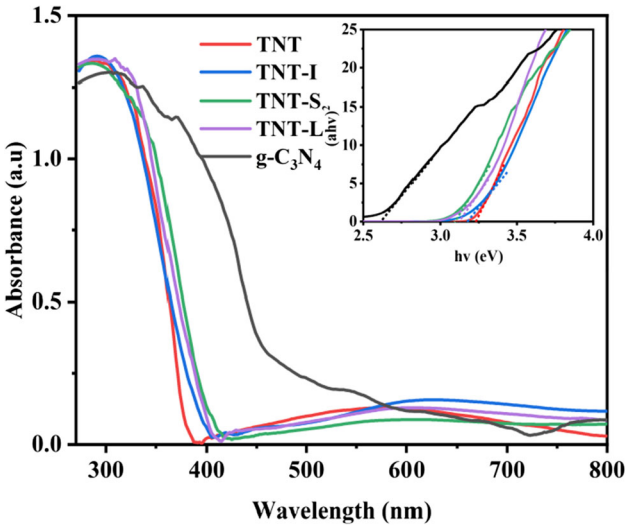

Figure 9 UV–vis diffuses reflectance spectra (DRS) of samples and inset of band-gaps.

according to the Kubelka–Munk function were 3.22, 3.17, 3.08, 3.11, and 2.63 eV, respectively [34, 35]. The composites showed a narrower bandgap than pure TiO_2, which implied the formation of TiO_2/g-C_3N_4 heterojunctions [36]. From the PL spectra (Fig. S4), the as-prepared g-C_3N_4/TiO_2composites exhibited weaker photoluminescence intensities than pure TiO_2, indicating that the modification of g-C_3N_4 inhibited photogenerated carrier recombination [37]. This result indicates that more electrons and holes are available for redox reactions, resulting in a higher photocurrent [38]. The degree of PL quenching was in accordance with the photoelectrochemical results.

Heterojunctions are always assembled of two semiconductor materials with staggered band structures. The difference in the work function between semiconductors will induce charge redistribution, which significantly affects charge separation and transfer. Therefore, it is imperative to study charge transfer mode in photocatalytic reactions. ESR spectra were used to detect the generation of •OH and $\bullet O_2^-$ radicals for understanding the charge transport process of TiO_2 and g-C_3N_4/TiO_2 heterojunction, and the results are shown in Fig. 10. No obvious peaks were observed for DMPO-•OH and DMPO-$\bullet O_2^-$ under darkness; after 10 min of irradiation, the signals of •OH and $\bullet O_2^-$ could be examined in both TNT and TNT-L samples [39, 40]. TNT-L showed a relatively stronger ESR signal than pure TiO_2 component. According to the conduction band (CB) and valence band (VB) positions of g-C_3N_4, the photogenerated holes cannot oxidize H_2O molecules to form •OH because the E_{VB} (1.57 eV) of g-C_3N_4 is lower than that of E (H_2O/•OH) (2.68 eV vs NHE, pH = 7) [41, 42]. There are two possible charge carrier migration mechanisms for g-C_3N_4/TiO_2 as shown in Fig. S5. For type-II heterojunction photocatalysts, photogenerated electrons from the CB of g-C_3N_4 could easily migrate to the CB of TiO_2, while the holes in the VB of TiO_2 would further transfer to the VB of g-C_3N_4, which led to the accumulation of electrons and holes in the CB of TiO_2 and VB of g-C_3N_4, respectively [43–45]. However, the Z-scheme heterojunction photocatalysts could drive the photogenerated electrons in the CB of TiO_2 to recombine directly with the holes in the VB of g-C_3N_4, while the excited electrons in the CB of g-$C_3N_4$and holes in the VB of TiO_2 are maintained and spatially separated [46, 47]. These two mechanisms are in favor of the generation and separation of charges in heterojunctions, so it is impossible to identify by electrochemical analysis [48]. If TNT-L was a type-II heterojunction, the ability to generate radicals would be weakened [49]. According to the ESR spectra of TNT-L, the enhanced signals of •OH and $\bullet O_2^-$ confirm that the construction of heterojunctions could promote the production of radicals, which contradicted the charge transfer mechanism of type-II heterojunction.

According to the experimental results discussed above, we proposed a possible PEC mechanism responsible for the g-C_3N_4/TiO_2 heterojunction, as shown in Fig. 11. Under full spectrum illumination, TiO_2 nanotubes and g-C_3N_4 can be simultaneously excited to generate photoinduced electrons and holes [50]. The excited electrons present in the conduction band of TiO_2 can rapidly combine with the holes from the valence band of g-C_3N_4 at the interface under built-in electric field driving. Thus, the electrons in the conduction band of g-C_3N_4 and the holes in the valence band of TiO_2 were effectively separated, thereby suppressing the recombination rate of charge carriers [51, 52]. Under an applied potential, these electrons were transmitted along the external circuit to the Pt electrode for the hydrogen evolution reaction. On the other hand, the remaining holes participated in the oxidation reaction to achieve the entire galvanic cycle [28, 53].

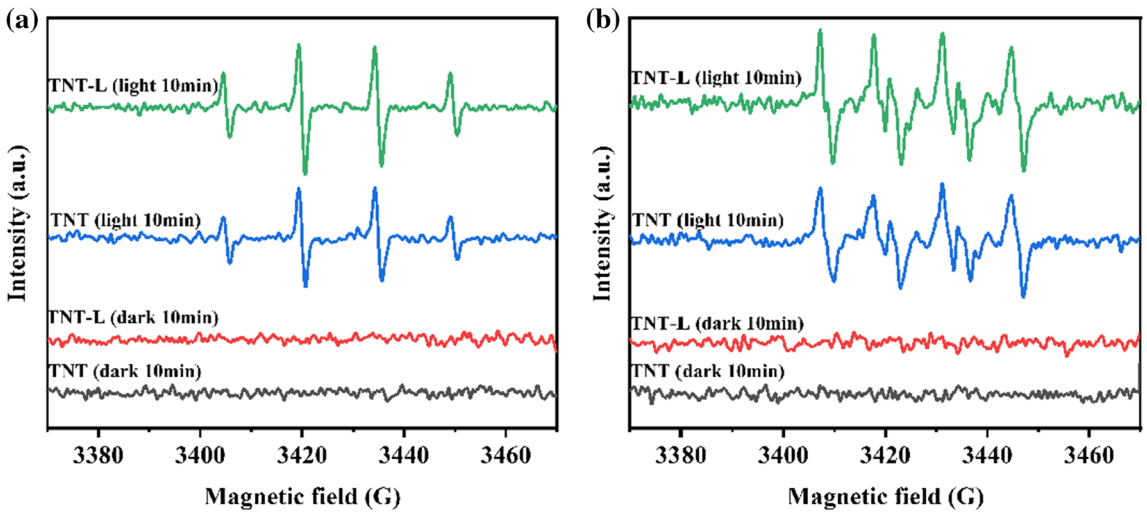

Figure 10 ESR spectra of DMPO-•OH (a), DMPO-$\bullet O_2^-$ (b) spin-trapping adducts in the photocatalytic system.

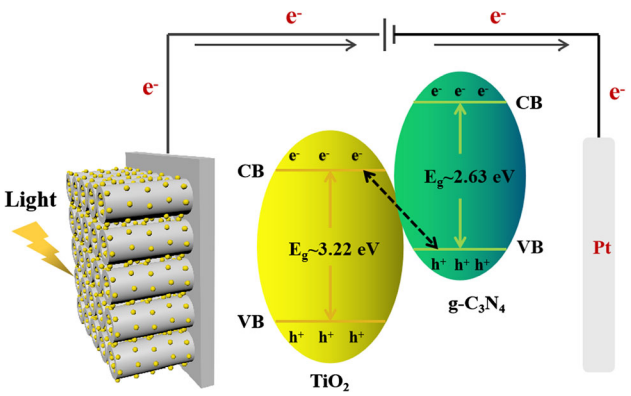

Figure 11 Schematic diagram of the photogenerated electron–hole separation for Z-scheme heterojunction.

Conclusion

In this study, three thermal polymerization approaches were used to fabricate heterojunctions by coupling g-C_3N_4 nanoparticles with one-dimensional TiO_2 nanotube arrays. Photoelectrochemical properties were investigated by linear sweep voltammetry, photocurrent response, and electrochemical impedance spectroscopy. Experimental results showed that the TNT-L photoanode possessed the highest PEC activity under solar irradiation, and the detection of ESR radicals confirmed the direct Z-scheme carrier transmission mechanism, leading to effective charge separation and enhanced redox ability. The results of this study describe a material that may be applicable to various photocatalytic applications.

Declarations

Conflict of interest The authors declare no conflict of interest.

Supplementary Information: The online version contains supplementary material available at https://doi.org/10.1007/s10853-022-07730-7.

References

[1] Acar C, Dincer I, Naterer GF (2016) Review of photocatalytic water-splitting methods for sustainable hydrogen production. Int J Energy Res 40:1449–1473

[2] Li X, Yu J, Jaroniec M (2016) Hierarchical photocatalysts. Chem Soc Rev 45:2603–2636

[3] Ye R, Fang H, Zheng YZ, Li N, Wang Y, Tao X (2016) Fabrication of CoTiO3/g-C3N4 hybrid photocatalysts with enhanced H2 evolution: Z-scheme photocatalytic mechanism insight. ACS Appl Mater Interfaces 8:13879–13889

[4] Zheng L, Ye X, Deng X, Wang Y, Zhao Y, Shi X, Zheng H (2020) Black phosphorus quantum dot-sensitized TiO2 nanotube arrays with enriched oxygen vacancies for efficient photoelectrochemical water splitting. ACS Sustain Chem Eng 8:15906–15914

[5] Xiao FX, Miao J, Tao HB, Hung SF, Wang HY, Yang HB, Chen J, Chen R, Liu B (2015) One-dimensional hybrid nanostructures for heterogeneous photocatalysis and photoelectrocatalysis. Small 11:2115–2131

[6] Wu J, Feng Y, Li D, Han X, Liu J (2019) Efficient photocatalytic CO2 reduction by P-O linked g-C3N4/TiO2-nanotubes Z-scheme composites. Energy 178:168–175

[7] Ren L, Huang S, Fan W, Liu T (2011) One-step preparation of hierarchical superparamagnetic iron oxide/graphene composites via hydrothermal method. Appl Surf Sci 258:1132–1138

[8] Wang XJ, Yang WY, Li FT, Zhao J, Liu RH, Liu SJ, Li B (2015) Construction of amorphous TiO(2)/BiOBr heterojunctions via facets coupling for enhanced photocatalytic activity. J Hazard Mater 292:126–136

[9] Wang X, Utsumi M, Yang Y, Li D, Zhao Y, Zhang Z, Feng C, Sugiura N, Cheng JJ (2015) Degradation of microcystin-LR by highly efficient AgBr/Ag3PO4/TiO2 heterojunction photocatalyst under simulated solar light irradiation. Appl Surf Sci 325:1–12

[10] Yao Y, Miao S, Liu S, Ma LP, Sun H, Wang S (2012) Synthesis, characterization, and adsorption properties of magnetic Fe3O4@graphene nanocomposite. Chem Eng J 184:326–332

[11] Xing G, Wu B, Chen S, Chua J, Yantara N, Mhaisalkar S, Mathews N, Sum TC (2015) Interfacial electron transfer barrier at compact TiO2 /CH3 NH3 PbI3 heterojunction. Small 11:3606–3613

[12] Zhou Q, Zhao D, Sun Y, Sheng X, Zhao J, Guo J, Zhou B (2020) g-C3N4- and polyaniline-co-modified TiO2 nanotube arrays for significantly enhanced photocatalytic degradation of tetrabromobisphenol A under visible light. Chemosphere 252:126468

[13] Min Y, Qi XF, Xu Q, Chen Y (2014) Enhanced reactive oxygen species on a phosphate modified C3N4/graphene photocatalyst for pollutant degradation. CrystEngComm 16:1287

[14] Zhang L, Liu D, Guan J, Chen X, Guo X, Zhao F, Hou T, Mu X (2014) Metal-free g-C 3 N 4 photocatalyst by sulfuric acid activation for selective aerobic oxidation of benzyl alcohol under visible light. Mater Res Bull 59:84–92

[15] Zhou L, Zhang H, Ji L, Shao Y, Li Y (2014) Fe3O4/MWCNT as a heterogeneous Fenton catalyst: degradation pathways of tetrabromobisphenol A. RSC Adv 4:24900–24908

[16] Liang X, Wang G, Huo T, Dong X, Wang G, Ma H, Liang H, Zhang X (2019) Band structure modification of g-C3N4 for efficient heterojunction construction and enhanced photocatalytic capability under visible light irradiation. Catal Commun 123:44–48

[17] Wei X, Shao C, Li X, Lu N, Wang K, Zhang Z, Liu Y (2016) Facile in situ synthesis of plasmonic nanoparticles-decorated g-C3N4/TiO2 heterojunction nanofibers and comparison study of their photosynergistic effects for efficient photocatalytic H2 evolution. Nanoscale 8:11034–11043

[18] Sun M, Shen S, Wu Z, Tang Z, Shen J, Yang J (2018) Rice spike-like g-C3N4/TiO2 heterojunctions with tight-binding interface by using sodium titanate ultralong nanotube as precursor and template. Ceram Int 44:8125–8132

[19] Zhang W, Song J, Wang D, Deng K, Wu J, Zhang L (2018) Dual interfacial modification engineering with p-type NiO nanocrystals for preparing efficient planar perovskite solar cells. J Mater Chem C 6:13034–13042

[20] Wang X, Maeda K, Thomas A, Takanabe K, Xin G, Carlsson JM, Domen K, Antonietti M (2009) A metal-free polymeric photocatalyst for hydrogen production from water under visible light. Nat Mater 8:76–80

[21] Nagaraja CM, Kaur M, Dhingra S (2020) Enhanced visible-light-assisted photocatalytic hydrogen generation by MoS2/g-C3N4 nanocomposites. Int J Hydrogen Energy 45:8497–8506

[22] Bashir H, Yi X, Yuan J, Yin K, Luo S (2019) Highly ordered TiO2 nanotube arrays embedded with g-C3N4 nanorods for enhanced photocatalytic activity. J Photochem Photobiol A 382:111930

[23] Wang H, Liang Y, Liu L, Hu J, Cui W (2018) Highly ordered TiO2 nanotube arrays wrapped with g-C3N4 nanoparticles for efficient charge separation and increased photoelectrocatalytic degradation of phenol. J Hazard Mater 344:369–380

[24] Lin Z, Yu B, Huang J (2020) Cellulose-derived hierarchical g-C3N4/TiO2-nanotube heterostructured composites with enhanced visible-light photocatalytic performance. Langmuir 36:5967–5978

[25] Sun B, Lu N, Su Y, Yu H, Meng X, Gao Z (2017) Decoration of TiO 2 nanotube arrays by graphitic-C 3 N 4 quantum dots with improved photoelectrocatalytic performance. Appl Surf Sci 394:479–487

[26] Alcudia-Ramos MA, Fuentez-Torres MO, Ortiz-Chi F, Espinosa-González CG, Hernández-Como N, García-Zaleta DS, Kesarla MK, Torres-Torres JG, Collins-Martínez V, Godavarthi S (2020) Fabrication of g-C3N4/TiO2 heterojunction composite for enhanced photocatalytic hydrogen production. Ceram Int 46:38–45

[27] Tiong P, Lintang HO, Endud S, Yuliati L (2015) Improved interfacial charge transfer and visible light activity of reduced graphene oxide–graphitic carbon nitride photocatalysts. RSC Adv 5:94029–94039

[28] Pandey B, Rani S, Roy SC (2020) A scalable approach for functionalization of TiO2 nanotube arrays with g-C3N4 for enhanced photo-electrochemical performance. J Alloy Compd 846:155881

[29] Athanasekou CP, Likodimos V, Falaras P (2018) Recent developments of TiO2 photocatalysis involving advanced oxidation and reduction reactions in water. J Envir Chem Eng 6:7386–7394

[30] Qing-kun X (2018) The effects of the electrochemical properties of pyrite by polypyrrole (PPy). Ferroelectrics 528:75–82

[31] Zhang SS, Tran DT (2015) Electrochemical verification of the redox mechanism of FeS2 in a rechargeable lithium battery. Electrochim Acta 176:784–789

[32] He J, Li Q, Chen Y, Xu C, Zhou K, Wang X, Zhang W, Li Y (2017) Self-assembled cauliflower-like FeS2 anchored into graphene foam as free-standing anode for high-performance lithium-ion batteries. Carbon 114:111–116

[33] Song C, Wang S, Dong W, Fang X, Shao J, Zhu J, Pan X (2016) Hydrothermal synthesis of iron pyrite (FeS 2) as efficient counter electrodes for dye-sensitized solar cells. Sol Energy 133:429–436

[34] Li X, Yu J, Low J, Fang Y, Xiao J, Chen X (2015) Engineering heterogeneous semiconductors for solar water splitting. J Mater Chem A 3:2485–2534

[35] Xia Y, He Z, Su J, Tang B, Hu K, Lu Y, Sun S, Li X (2018) Fabrication of magnetically separable NiFe2O4/BiOI nanocomposites with enhanced photocatalytic performance under visible-light irradiation. RSC Adv 8:4284–4294

[36] Peng G, Zhang M, Deng S, Shan D, He Q, Yu G (2018) Adsorption and catalytic oxidation of pharmaceuticals by nitrogen-doped reduced graphene oxide/Fe3O4 nanocomposite. Chem Eng J 341:361–370

[37] Ye C, Li J-X, Li Z-J, Li X-B, Fan X-B, Zhang L-P, Chen B, Tung C-H, Wu L-Z (2015) Enhanced driving force and charge separation efficiency of protonated g-C3N4 for photocatalytic O2 evolution. ACS Catal 5:6973–6979

[38] Ye L, Wang D, Chen S (2016) Fabrication and enhanced photoelectrochemical performance of MoS(2)/S-doped g-C(3)N(4) heterojunction film. ACS Appl Mater Interfaces 8:5280–5289

[39] Li P, Guo J, Ji X, Xiong Y, Lai Q, Yao S, Zhu Y, Zhang Y, Xiao P (2021) Construction of direct Z-scheme photocatalyst by the interfacial interaction of WO3 and SiC to enhance the redox activity of electrons and holes. Chemosphere 282:130866

[40] Zhang F, Liu J, Yue H, Cheng G, Xue X (2021) Enhanced photo-Fenton catalytic activity by spherical FeS2 nanoparticles and photoelectric property of hybrid FeS2/rGO. Vacuum 192:110433

[41] Li X, Garlisi C, Guan Q, Anwer S, Al-Ali K, Palmisano G, Zheng L (2021) A review of material aspects in developing direct Z-scheme photocatalysts. Mater Today 47:75–107

[42] Ge L, Han C, Liu J (2011) Novel visible light-induced g-C3N4/Bi2WO6 composite photocatalysts for efficient degradation of methyl orange. Appl Catal B 108–109:100–107

[43] Jiang W, Zong X, An L, Hua S, Miao X, Luan S, Wen Y, Tao FF, Sun Z (2018) Consciously constructing heterojunction or direct Z-scheme photocatalysts by regulating electron flow direction. ACS Catal 8:2209–2217

[44] Di Liberto G, Tosoni S, Pacchioni G (2021) Z-Scheme versus type-II junction in g-C3N4/TiO2 and g-C3N4/SrTiO3/TiO2 heterostructures, Catalysis. Sci Technol 11:3589–3598

[45] Li L, Li L, Sun T, Yu X, Long L, Xu L, Yan J (2019) Novel H3PW12O40/TiO2-g-C3N4 type-II heterojunction photocatalyst with enhanced visible-light photocatalytic properties. J Solid State Chem 274:152–161

[46] Xu Q, Zhang L, Yu J, Wageh S, Al-Ghamdi AA, Jaroniec M (2018) Direct Z-scheme photocatalysts: principles, synthesis, and applications. Mater Today 21:1042–1063

[47] Lu L, Wang G, Zou M, Wang J, Li J (2018) Effects of calcining temperature on formation of hierarchical TiO2/g-C3N4 hybrids as an effective Z-scheme heterojunction photocatalyst. Appl Surf Sci 441:1012–1023

[48] Wang J, Xia Y, Zhao H, Wang G, Xiang L, Xu J, Komarneni S (2017) Oxygen defects-mediated Z-scheme charge separation in g-C3N4/ZnO photocatalysts for enhanced visible-light degradation of 4-chlorophenol and hydrogen evolution. Appl Catal B 206:406–416

[49] Zhu L, Li H, Xia P, Liu Z, Xiong D (2018) Hierarchical ZnO Decorated with CeO2 Nanoparticles as the Direct Z-Scheme Heterojunction for Enhanced Photocatalytic Activity. ACS Appl Mater Interfaces 10:39679–39687

[50] Wang J, Wang G, Wang X, Wu Y, Su Y, Tang H (2019) 3D/2D direct Z-scheme heterojunctions of hierarchical TiO2 microflowers/g-C3N4 nanosheets with enhanced charge carrier separation for photocatalytic H2 evolution. Carbon 149:618–626

[51] Liu J, Cheng B, Yu J (2016) A new understanding of the photocatalytic mechanism of the direct Z-scheme g-C3N4/TiO2 heterostructure. Phys Chem Chem Phys 18:31175–31183

[52] Huang Z, Jia S, Wei J, Shao Z (2021) A visible light active, carbon–nitrogen–sulfur co-doped TiO2/g-C3N4 Z-scheme heterojunction as an effective photocatalyst to remove dye pollutants. RSC Adv 11:16747–16754

[53] Yang M, Liu J, Zhang X, Qiao S, Huang H, Liu Y, Kang Z (2015) C3N4-sensitized TiO2 nanotube arrays with enhanced visible-light photoelectrochemical performance. Phys Chem Chem Phys 17:17887–17893